

Tibetan plateau aridification linked to global cooling at the Eocene–Oligocene transition

Guillaume Dupont-Nivet¹, Wout Krijgsman¹, Cor G. Langereis¹, Hemmo A. Abels², Shuang Dai³ & Xiaomin Fang^{3,4}

Continental aridification and the intensification of the monsoons in Asia are generally attributed to uplift of the Tibetan plateau and to the land–sea redistributions associated with the continental collision of India and Asia^{1–3}, whereas some studies suggest that past changes in Asian environments are mainly governed by global climate^{4–6}. The most dramatic climate event since the onset of the collision of India and Asia is the Eocene–Oligocene transition, an abrupt cooling step associated with the onset of glaciation in Antarctica 34 million years ago^{7–9}. However, the influence of this global event on Asian environments is poorly understood. Here we use magnetostratigraphy and cyclostratigraphy to show that aridification, which is indicated by the disappearance of playa lake deposits in the northeastern Tibetan plateau, occurred precisely at the time of the Eocene–Oligocene transition. Our findings suggest that this global transition is linked to significant aridification and cooling in continental Asia recorded by palaeontological and palaeoenvironmental changes^{10–12}, and thus support the idea that global cooling is associated with the Eocene–Oligocene transition^{13–15}. We show that, with sufficient age control on the sedimentary records, global climate can be distinguished from tectonism and recognized as a major contributor to continental Asian environments.

Global climate and regional tectonism affect palaeoenvironmental conditions that are recorded during the deposition and accumulation of sediments¹⁶. In Asia, climate models^{1,3} have shown that uplift of the Tibetan plateau and retreat of the Paratethys epicontinental sea associated with the Indo-Asia collision during the Cenozoic era can result in monsoonal intensification, continental aridification and increased erosion. When recognized in the sedimentary records, these palaeoenvironmental conditions have thus been attributed to regional tectonism, although they can equally well indicate global climate changes^{4–6}. The key to distinguishing climatic effects from those of tectonism is to date the regional expression of these processes in the geologic record with sufficient resolution and accuracy to enable correlation to global climatic events precisely calibrated in the marine realm. The exceptionally long (~30 million years, Myr) continuous sedimentary succession of the Xining basin¹⁷ at the northeastern margin of the Tibetan plateau provides an excellent opportunity to study the sedimentary signature of tectonic and climatic processes during Eocene to Oligocene times. The stratigraphic sequence reveals a remarkably sharp and widespread change in depositional environment expressed regionally by the disappearance of massive gypsum layers. To determine the cause of this lithologic change, detailed lithofacies analyses and high-resolution dating were performed on two parallel sedimentary sections from the Xining basin (the Shuiwan and Xiejia sections; Fig. 1).

The lower part of the stratigraphy studied consists of regular alternations of laterally continuous gypsum layers and red mudstone beds

(Fig. 2). The red mudstone intervals consist of silty clay virtually devoid of sedimentary structures, suggesting alteration during extended sub-aerial exposure after sheet-flood events supplied the clastic mud. They are typical of a distal alluvial fan environment¹⁶. Gypsiferous intervals are decimetre- to metre-thick tabular, nodular or laminar beds of alabastrine massive gypsum showing some chick-enwire structures and displacive enterolithic veins (Fig. 1). They can grade laterally into green mudstone with preserved lacustrine lamination and are indicative of various stages of chemical precipitation in a playa lake environment¹⁶ (see Supplementary Table 1). The precipitation of evaporites in continental playa-type systems is

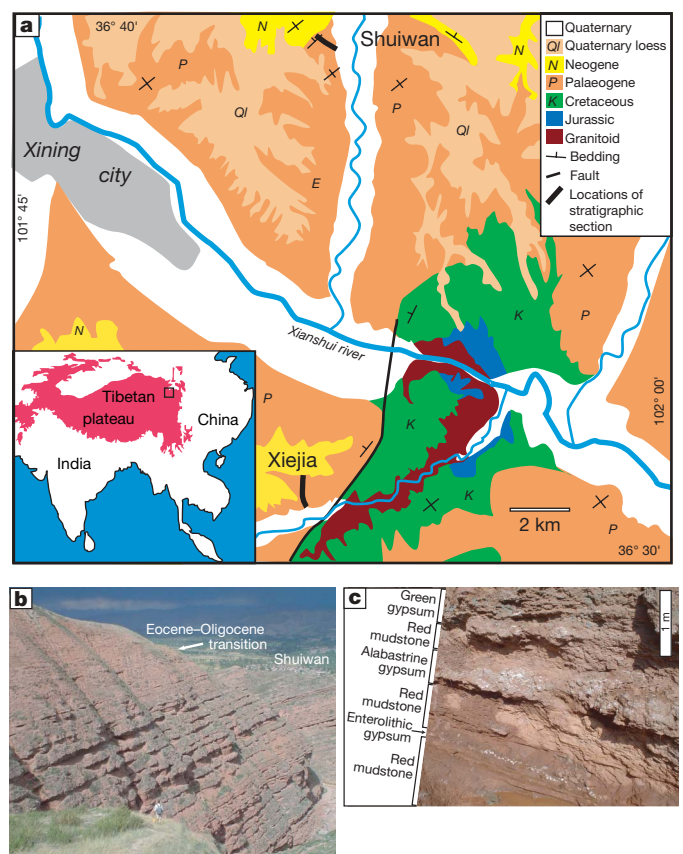


Figure 1 | Geologic setting. **a**, Location of studied stratigraphic sections. **b**, Field view to northeast, showing part of the Shuiwan section, including the end of cyclic gypsiferous deposition at the Eocene–Oligocene transition. **c**, Typical gypsum–mudstone cyclic alternations displaying characteristic lithofacies described in the text.

¹Paleomagnetic Laboratory 'Fort Hoofddijk', Department of Earth Sciences, Utrecht University, Budapestlaan 17, ²Stratigraphy–Paleontology, Department of Earth Sciences, Utrecht University, Budapestlaan 4, 3584 CD Utrecht, The Netherlands. ³Lanzhou University, Key Laboratory of Western China's Environmental Systems, Gansu 730000, China. ⁴Institute of Tibetan Plateau Research, Chinese Academy of Science, P O Box 2871, Beijing 100085, China.

chiefly determined by the supply of drained atmospheric water, ultimately providing solutes through groundwater inflow and overland runoff¹⁸. Gypsum intercalations within the red mudstones are thus indicative of periods with significantly higher water supply providing sufficient solutes to accumulate metre-scale gypsum layers¹⁸. The regularity of the gypsum/mudstone alternations indicate periodical fluctuations in atmospheric water supply to the basin, suggesting a cyclic mechanism most probably controlled by climate oscillations.

In the upper part of the stratigraphy, fully developed gypsum layers disappear. Sediments are dominated by homogenous red mudstones with minor interstitial gypsum content and occasional sandstone layers indicative of a distal alluvial fan depositional environment, without playa lake intercalations. The inhibition of gypsum accumulation between the lower and the upper part of the stratigraphy implies a permanent drop in the supply of atmospheric water that resulted in pronounced aridification of the Xining basin.

Consistent with this, regional palaeoenvironmental records also document aridification in the Eocene to Oligocene interval considered here. The fossil pollen records from the studied sediments of the Xining basin¹⁹ indicate a drying and cooling environment, as indicated by an increase in herbs and conifers. North of the Tibetan plateau, an abrupt faunal turnover is linked to cooling and aridification, as indicated by the evolution of mammal tooth patterns and a drastic size decrease from large Eocene species (including some of the largest terrestrial mammals ever known) to small Oligocene species

dominated by rodents¹⁰. Moreover, the first extensive set of $\delta^{18}\text{O}$ and $\delta^{13}\text{C}$ isotopic data reveals a positive shift between Eocene and Oligocene continental strata that has been attributed to aridification¹².

To determine whether this aridification can be linked to tectonism or known climatic events in the Eocene to Oligocene interval, we accurately dated the sediments. Magnetostratigraphic sampling of the two sections was performed to determine the pattern of normal and reversed polarity intervals of the Earth's palaeomagnetic field. Palaeomagnetic analysis (see Methods and Supplementary Information) and the excellent consistency between the two records indicate a primary origin of the rock magnetization and the reliability of polarity intervals (Fig. 2). Our results improve and corroborate the long magnetostratigraphic records previously obtained from the Xining basin¹⁷, showing a distinctive pattern of two long reversed intervals (R1 and R2) separated by a shorter normal interval (N2). This pattern provides a unique correlation to chrons C12r and C13r of the geomagnetic polarity timescale (GPTS²⁰), which indicates that the sampled interval straddles the Eocene–Oligocene boundary, in agreement with palaeontological constraints^{17,19} (see Methods). According to the GPTS correlation, the average period of gypsum–mudstone alternations is 109 thousand years (109 kyr) at Xiejia and 93 kyr at Shuiwan. These values are consistent with the ~ 100 -kyr periodicity of the Earth's orbital eccentricity, suggesting that the supply of atmospheric water, periodically sufficient for gypsum

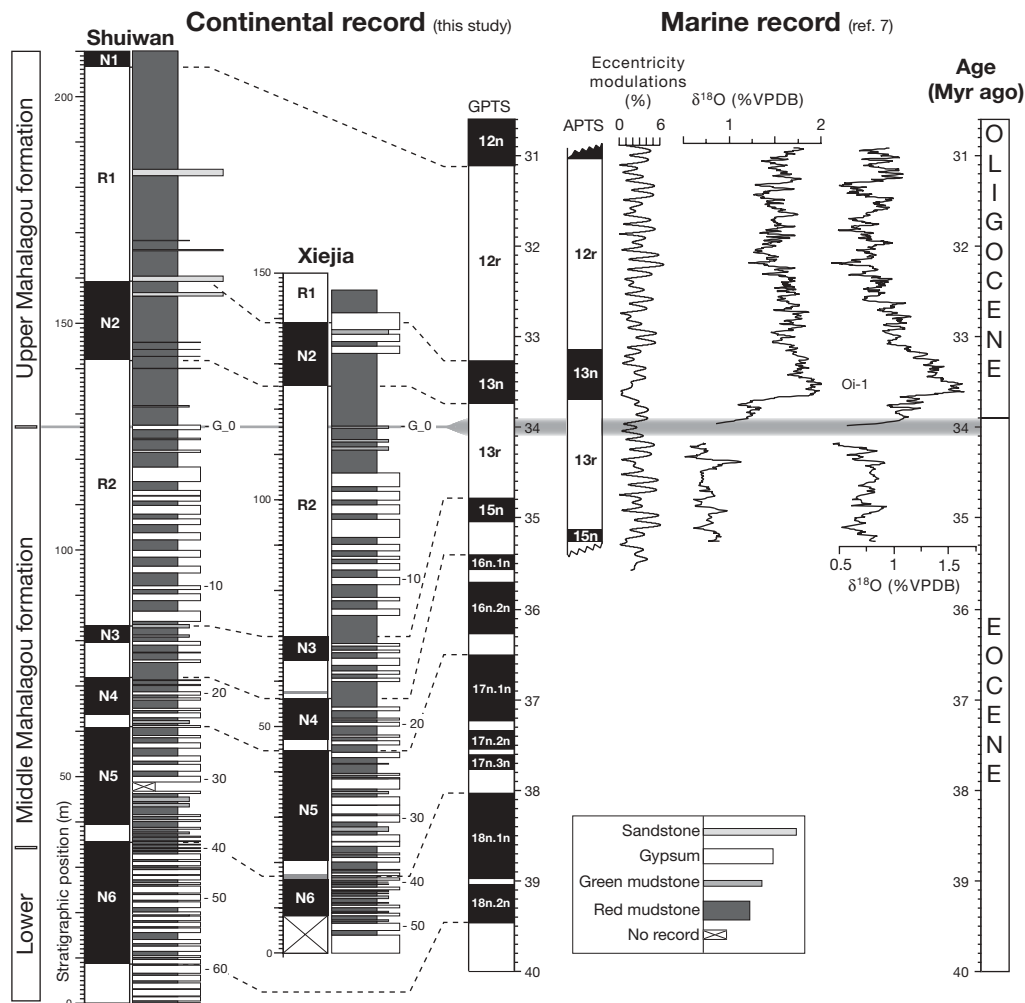


Figure 2 | Stratigraphic correlations. Lithostratigraphic descriptions are given in metres from the bottom of the Shuiwan and Xiejia sections. Eccentricity-driven gypsum–mudstone cycles are numbered down from the highest correlatable level G_0 at the lithofacies change. Observed normal (N)

and reverse (R) polarity zones (N1 to N6) are correlated to chrons of the GPTS²⁰ and the APTS⁷. Eccentricity modulation model is from ref. 22. The stable isotope shift is from the marine record at the Eocene–Oligocene transition⁷. VPDB, Vienna Pee-Dee Belemnite standard.

deposition, was controlled by eccentricity-driven climate variability. Pronounced aridification is defined by the interruption of this periodic system of basin-wide gypsum generation, above the highest gypsiferous level correlatable between the two sections (G₀ on Fig. 2). This layer marks the end of the distinctive pattern of regular gypsum–mudstone cycles, followed by mudstone-dominated successions with occasional non-correlative sandy and gypsiferous levels. In both sections, G₀ occurs near the top of C13r. Using linear interpolation between GPTS chron boundaries, G₀ is estimated at 34 Myr ago (33.9 Myr ago at Xiejia and 34.0 Myr ago at Shuiwan, Supplementary Table 4).

This age corresponds well with the most important step in Cenozoic global cooling 34 Myr ago, characterized by the onset of permanent Antarctic ice sheets at the Eocene–Oligocene transition and marked in the marine records by an abrupt increase in $\delta^{18}\text{O}$ and $\delta^{13}\text{C}$ values (the Oi-1 event)^{7–9,21} (Fig. 2). This marine isotope increase was recently precisely documented as a two-step shift (40 kyr each) separated by an intermediate plateau (200 kyr)⁷. To formally compare our results with this marine record, we calibrate our data to the astronomically tuned polarity timescale (APTS) of this study⁷, providing chron boundaries dated with respect to the variation of Earth's orbital parameters²². Linear interpolation between these chron boundaries also indicates a 34-Myr age for G₀ (33.9 at Xiejia and 34.1 at Shuiwan; Supplementary Table 4). Furthermore, the recognized eccentricity forcing of the gypsum–mudstone cyclicity enables us to test the consistency of our records directly with the astronomically tuned marine record. The number of eccentricity cycles expected to separate G₀ from the underlying chron C15n—according to the APTS—is indeed consistent at both sections with the number of observed gypsum–mudstone alternations separating G₀ from N3 (13 alternations at Shuiwan and Xiejia). This result independently validates our age estimate for G₀ at 34 Myr ago, indicating that the start of aridification after G₀ is coeval with the marine isotope shift of the climate transition (Fig. 2).

This remarkable correlation provides the first direct link between the Eocene–Oligocene climate transition and the aridification of continental Asia. In view of this finding, existing Eocene–Oligocene records of Asian environments must be interpreted with respect to climate change. The positive $\delta^{18}\text{O}$ and $\delta^{13}\text{C}$ shifts recorded north of the Tibetan plateau¹² can be attributed to the combined effects of aridification and the positive shift in isotopic values of ocean water (the ultimate source of meteoric water) at the Eocene–Oligocene transition. Abrupt changes in the Asian fauna in response to cooling and aridification (the Mongolian Remodelling)¹⁰ can now be confidently linked to the Eocene–Oligocene transition and correlated to the large mammalian turnover in Europe (the 'Grande Coupure'), as well as globally reported continental and marine records of comparable faunal and floral turnovers at this time^{13,21}. This supports the paradigm that the Eocene–Oligocene transition is associated with global atmospheric cooling and contrasts with recent claims, based on a few localized continental palaeotemperature estimates, that it may be linked to changes in Antarctic ice volume only^{14,15}. Records of cooling and aridification^{10–12,19} in the Asian interior are thus attributed to cooling of global ocean temperatures, reducing moisture supply to continental interiors. This effect may have been enhanced by a large Paratethys retreat induced by glacio-eustatic sea level lowering driven by Antarctic glaciation. Lastly, increasing sediment accumulation recorded over the East and Southeast Asian offshore region at about 33 Myr ago²³ now suggests that Eocene–Oligocene global cooling was also associated with increased regional erosion and sediment transport to the sea.

Our study demonstrates that global climate cooling must be recognized as a major contributor to Asian palaeoenvironment. It substantiates previous propositions that Pliocene climate deterioration or late Miocene global cooling essentially governed Asian depositional environments^{4–6}. The growing evidence that global cooling is associated with continental aridification along with intensification of

monsoons and increased regional erosion remains to be tested by climate models. General circulation models have mainly focused on the effect of regional tectonism on Asian and global climate^{1,3,24}, showing that Tibetan uplift and Paratethys retreat can also increase Asian continental aridity, monsoons and erosion. Ultimately, Tibetan uplift can lead to global cooling through atmospheric circulation perturbations and carbon dioxide lowering associated with increased rock weathering²⁵.

Our results do not exclude that, in conjunction with the Eocene–Oligocene transition, tectonic processes have also contributed to Asian palaeoclimatic conditions. However, to establish the importance of these processes in driving Asian or global climate at this time, improved age control on their sedimentary expression is required. The Paratethys retreat is bracketed between late Eocene and latest Miocene time²⁶ and estimates for Tibetan plateau uplift range from the early Cenozoic at least 35 Myr ago^{27,28} to the Pliocene 2–4 Myr ago¹. In time, accurate and precise dating of Tibetan uplift may finally confirm the hypothesis that it was the primary cause of the Eocene–Oligocene climate transition through global atmospheric carbon dioxide lowering, instead of the recently challenged paradigm that the Eocene–Oligocene transition was triggered by the opening of a sea passage around Antarctica^{7–9,29}. Our study illustrates that distinguishing climate effects from tectonism can be accomplished by high-resolution dating, using magnetostratigraphy validated independently by the study of orbitally driven cyclicity in sediments³⁰. This seems a promising tool for Asian sedimentary records, which often show cyclicity but are devoid of volcanics for radiometric calibration.

METHODS

Palaeomagnetic analysis. Palaeomagnetic sampling was performed in the course of two field seasons using a standard portable coring device; 187 and 110 sampling levels were collected in the 209.5-m-thick Shuiwan section and the 145.8-m-thick Xiejia section respectively (average sampling interval of 1.2 m). Palaeomagnetic analysis yielded reliable primary characteristic remanent magnetization directions at 206 levels (see Supplementary Figures 1 and 2 and Supplementary Tables 2 and 3). Polarity zones at the Shuiwan (12 zones) and Xiejia (10 zones) sections are defined by palaeomagnetic directions from three or more levels (Supplementary Fig. 3). Two questionable short polarity zones are defined by one sample only (depicted in grey on Fig. 2). Apart from these short intervals, the excellent consistency between the two magnetostratigraphic records strongly confirms the primary origin of the rock magnetization and the reliability of polarity intervals.

Palaeontological constraints. Palaeontological constraints provide a starting point for our age model (see palaeontological references in ref. 17). A relatively rich record of fossil mammals, ostracods, charophytes and pollen have been collected at the location of the two sampled sections (Xiejia and Shuiwan) including the Mahalagou formation (of interest for this study), the underlying Honggou formation, and the overlying Xiejia formation. The upper part of the Xiejia formation contains a well-documented mammal assemblage (the Xiejia fauna) that is described to be from the lowermost Miocene age (>20 Myr ago), implying that most of the Xiejia formation below this fossil locality is of Oligocene age. In addition, the lower part of the Xiejia formation is ascribed a late Oligocene age, the Mahalagou formation an early Oligocene age and the Honggou formation an Eocene age, on the basis of ostracods, charophytes and (mostly) pollen records¹⁹. Taken together, existing palaeontological constraints point to an early Oligocene age assignment for the sampled strata in the Mahalagou formation.

Magnetostratigraphic correlation. The complete pattern of magnetic polarity zones from the Honggou, Mahalagou and Xiejia formations recorded at the Xiejia and Shuiwan sections is provided by ref. 17. From this long record, two long reversed polarity zones separated by a shorter normal zone stand out clearly within the Mahalagou formation. Our focused palaeomagnetic sampling and analysis of this characteristic interval confirms this pattern and excludes the occurrences of the questionable short normal polarity intervals reported in the Xiejia section¹⁷. Above and below the pair of long reversed polarity zones are numerous shorter zones. When compared to the GPTS, the Early Oligocene to Late Eocene time interval is characterized by two long reversed chrons (C12r and C13r) separated by a shorter normal chron (C13n). Above and below this pair of long reversed chrons, the GPTS indicates shorter chrons. Given the palaeontological constraints and the pattern of magnetic polarity zones, the simplest

interpretation is to correlate the pair of long reversed polarity zones of the Mahalagou formation to the pair of reversed polarity chrons (C12r and C13r).

Although the shorter length of R1 relative to R2 is inverse to the pattern of C12r–C13r in the GPTS, alternative correlations of this pair of long reversed intervals are practically impossible. Correlating the long observed reversed intervals higher on the GPTS where the reversal rate is high would imply, at least, an order-of-magnitude increase in accumulation rates, fortuitously during the duration of these chrons. Correlation below would require these long reversed chrons to be expressed higher up in the section, where recorded polarity zones are short, ultimately implying at least an order-of-magnitude decrease in accumulation rates. Such large variations would probably be indicated by facies variations (for example, conglomerates, disconformity or unconformity) that are not observed.

Below R2, we correlate N3 to C15n, N4 to C16n.1n–C16.2n, N5 to C17n.1n–C17n.2n–C17n.3n and N6 to C18n.1n–C18n.2n (Fig. 2). Supporting these correlations are the resulting consistent sedimentation rates calculated by linear interpolation between these chron boundaries (Supplementary Table 4). However, this correlation implies that four short reversed intervals have not been detected: C16n.1r = 159 kyr; C17n.1r = 131 kyr; C17n.2r = 72 kyr; and C18n.1r = 79 kyr. Given the low sedimentation rates, we argue that the following can explain the absence of these short intervals: (1) insufficient sampling resolution (average 1.2 m); (2) the absence of sampling in gypsum intervals yielding no palaeomagnetic signal; and (3) possible gaps in such sub-aerial deposits. An alternative in which no chrons are missed may be considered by correlating N5 to C16n.2n and N6 to C17n.1n. This alternative correlation would not change the magnetostratigraphic correlation of G₀ within C13r but we discarded it because the expected long normal interval C18n is not observed below N6 in the existing record¹⁷, which shows instead a long reversed interval.

Received 25 July; accepted 5 December 2006.

- An, Z., Kutzbach, J. E., Prell, W. L. & Porter, S. C. Evolution of Asian monsoons and phased uplift of the Himalaya–Tibetan plateau since Late Miocene times. *Nature* **411**, 62–66 (2001).
- Guo, Z. T. *et al.* Onset of Asian desertification by 22 Myr ago inferred from loess deposits in China. *Nature* **416**, 159–163 (2002).
- Ramstein, G., Fluteau, F., Besse, J. & Joussaume, S. Effect of orogeny, plate motion and land–sea distribution on Eurasian climate change over the past 30 million years. *Nature* **386**, 788–795 (1997).
- Gupta, A. K., Singh, R. K., Joseph, S. & Thomas, E. Indian Ocean high-productivity event (10–8 Ma): Linked to global cooling or to the initiation of the Indian monsoons? *Geology* **32**, 753–756 (2004).
- Molnar, P. Late Cenozoic increase in accumulation rates of terrestrial sediments: How might climate change have affected erosion rates? *Annu. Rev. Earth Planet. Sci.* **32**, 67–89 (2004).
- Zhang, P., Molnar, P. & Downs, W. Increased sedimentation rates and grain sizes 2–4 Myr ago due to the influence of climate change on erosion rates. *Nature* **410**, 891–897 (2001).
- Coxall, H. K., Wilson, P. A., Palike, H., Lear, C. H. & Backman, J. Rapid stepwise onset of Antarctic glaciation and deeper calcite compensation in the Pacific Ocean. *Nature* **433**, 53–57 (2005).
- DeConto, R. M. & Pollard, D. Rapid Cenozoic glaciation of Antarctica induced by declining atmospheric CO₂. *Nature* **421**, 245–249 (2003).
- Zachos, J. C. & Kump, L. R. Carbon cycle feedbacks and the initiation of Antarctic glaciation in the earliest Oligocene. *Glob. Planet. Change* **47**, 51–66 (2005).
- Meng, J. & McKenna, M. C. Faunal turnovers of Palaeogene mammals from the Mongolian Plateau. *Nature* **394**, 364–367 (1998).
- Garzzone, C., Ikari, M. J. & Basu, A. R. Source of Oligocene to Pliocene sedimentary rocks in the Linxia basin in northeastern Tibet from Nd isotopes: Implications for tectonic forcing of climate. *Geol. Soc. Am. Bull.* **117**, 1156–1166, doi:10.1130/B25743.1 (2005).
- Graham, S. A. *et al.* Stable isotope records of Cenozoic climate and topography, Tibetan plateau and Tarim basin. *Am. J. Sci.* **305**, 101–118 (2005).
- Ivany, L. C., Patterson, W. P. & Kyger, C. L. Cooler winters as a possible cause of mass extinctions at the Eocene/Oligocene boundary. *Nature* **407**, 887–890 (2000).
- Grimes, S. T., Hooker, J. J., Collinson, M. E. & Matthey, D. P. Summer temperatures of late Eocene to early Oligocene freshwaters. *Geology* **33**, 189–192 (2005).
- Kohn, M. J. *et al.* Climate stability across the Eocene–Oligocene transition, southern Argentina. *Geology* **32**, 621–624 (2004).
- Talbot, M. R. & Allen, P. A. in *Sedimentary Environments: Processes, Facies and Stratigraphy* (ed. Reading, H. G.) 83–124 (Blackwell Publishing Inc., Oxford, 1996).
- Dai, S. *et al.* Magnetostratigraphy of Cenozoic sediments from the Xining Basin: Tectonic implications for the northeastern Tibetan Plateau. *J. Geophys. Res.* **111**, doi:10.1029/2005JB004187 (2006).
- Yechieli, Y. & Wood, W. W. Hydrogeologic processes in saline systems: playas, sabkhas and saline lakes. *Earth Sci. Rev.* **58**, 343–365 (2002).
- Wang, D.-N., Sun, X.-Y. & Zhao, Y.-N. Late Cretaceous to Tertiary palynofloras in Xinjiang and Qinghai, China. *Rev. Palaeobot. Palynol.* **65**, 95–104 (1990).
- Ogg, J. G. & Smith, A. G. in *A Geologic Time Scale 2004* (eds Gradstein, F. M., Ogg, J. G. & Smith, A. G.) 63–86 (Cambridge Univ. Press, Cambridge, UK, 2004).
- Prothero, D. R. in *Encyclopedia of Geology* (eds Selley, R., Cocks, R. & Plimer, I.) 472–478 (Elsevier, London, 2004).
- Laskar, J. *et al.* A long-term numerical solution for the insolation quantities of the Earth. *Astron. Astrophys.*, doi:10.1051/0004-6361:20041335 (2004).
- Clift, P. D., Layne, G. D. & Blusztajn, J. Marine sedimentary evidence for monsoon strengthening, Tibetan uplift and drainage evolution in Asia. Continent–ocean interactions in the East Asian marginal seas. *AGU Monogr.* **149**, 255–282 (2004).
- Kutzbach, J. E. & Behling, P. Comparison of simulated changes of climate in Asia for two scenarios: Early Miocene to present, and present to future enhanced greenhouse. *Glob. Planet. Change* **41**, 157–165 (2004).
- Ruddiman, W. F., Kutzbach, J. E. & Prentice, I. C. in *Tectonic Uplift and Climate Change* (ed. Ruddiman, W. F.) 203–235 (Plenum, New York, 1997).
- Popov, S. *et al.* Lithological–paleogeographic maps of Paratethys 10 maps Late Eocene to Pliocene. *Courier Forschungsinstitut Senckenberg* **250**, 1–42 (2004).
- Rowley, D. B. & Currie, B. S. Palaeo-altimetry of the late Eocene to Miocene Lunpola basin, central Tibet. *Nature* **439**, 677–681 (2006).
- Harris, N. B. W. The elevation history of the Tibetan Plateau and its implications for the Asian monsoon. *Palaeogeogr. Palaeoclimatol. Palaeoecol.* **241**, 4–15 (2006).
- Huber, M. *et al.* Eocene circulation of the Southern Ocean: Was Antarctica kept warm by subtropical waters? *Paleoceanography* **19**, doi:10.1029/2004PA001014 (2004).
- Krijgsman, W. *et al.* Revised astrochronology for the Ain el Beida section (Atlantic Morocco): No glacio-eustatic control for the onset of the Messinian Salinity Crisis. *Stratigraphy* **1**, 87–101 (2004).

Supplementary Information is linked to the online version of the paper at www.nature.com/nature.

Acknowledgements Reviews by C. Garzzone and discussions with F. Hilgen and M. Szurlies greatly improved the original manuscript. We thank H. Pälike and P. Wilson for sharing chron age calibrations. Lanzhou University students Dang Y. and Meng Q. provided logistical assistance. This project was funded through a 'Marie Curie' Fellowship from the European Union and a 'Veni' grant from the Netherlands science foundation (NWO) to G.D.-N.

Author Information Reprints and permissions information is available at www.nature.com/reprints. The authors declare no competing financial interests. Correspondence and requests for materials should be addressed to G.D.-N. (gdn@ge.uu.nl).

Supplementary Information

Tibetan Plateau aridification linked to global cooling at the Eocene-Oligocene transition

Guillaume Dupont-Nivet, Wout Krijgsman, Cor G. Langereis, Hemmo A. Abels ,
Shuang Dai & Xiaomin Fang

Nature 05516.

Guide to Supplementary Information

Supplementary figures and legends

p. 2-4

Supplementary Figure 1. Characteristic thermal demagnetisation behaviours.	p. 2
Supplementary Figure 2. Characteristic remanent magnetization (ChRM) directions and field tests applied to both sections.	p. 3
Supplementary Figure 3. Magnetostratigraphy and lithostratigraphy of Shuiwan and Xiejia sections.	p. 4

Supplementary tables

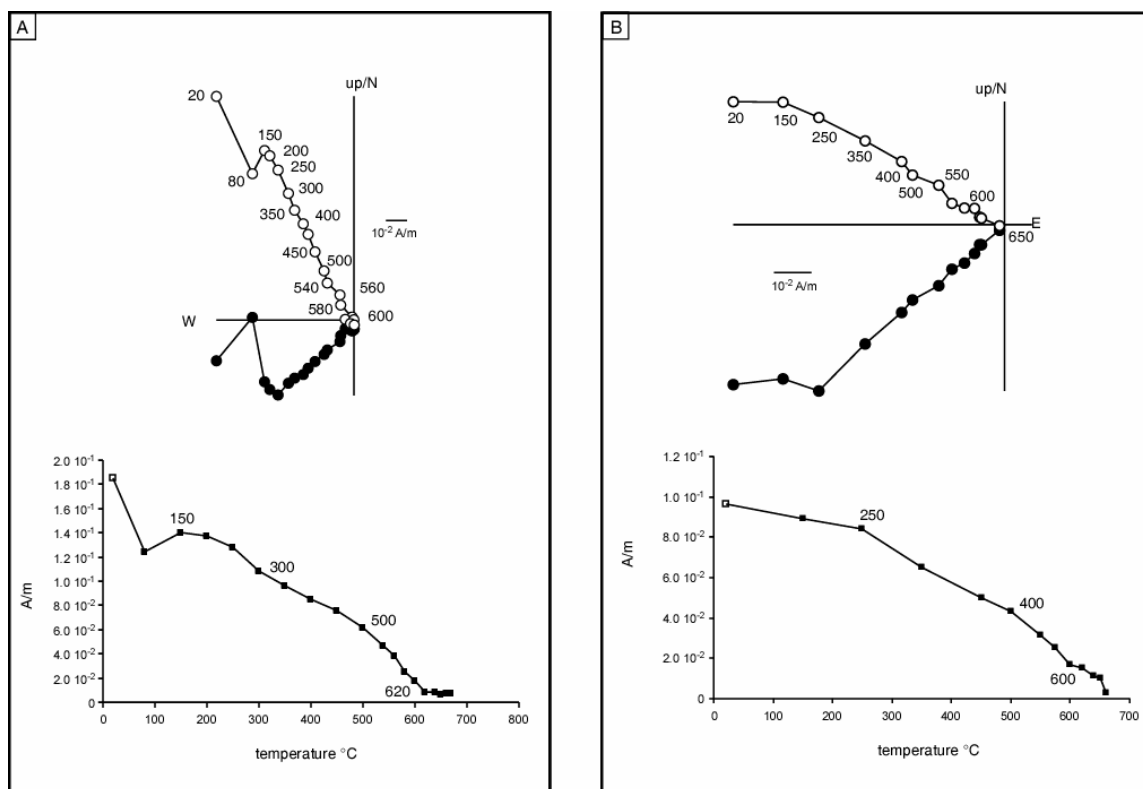
p. 5-11

Supplementary Table 1. Lithofacies description and depositional environments.	p. 5
Supplementary Table 2. Shuiwan section ChRM directions.	p. 6-8
Supplementary Table 2. Shuiwan section ChRM directions.	p. 9-10
Supplementary Table 4. Correlations and rates.	p. 11

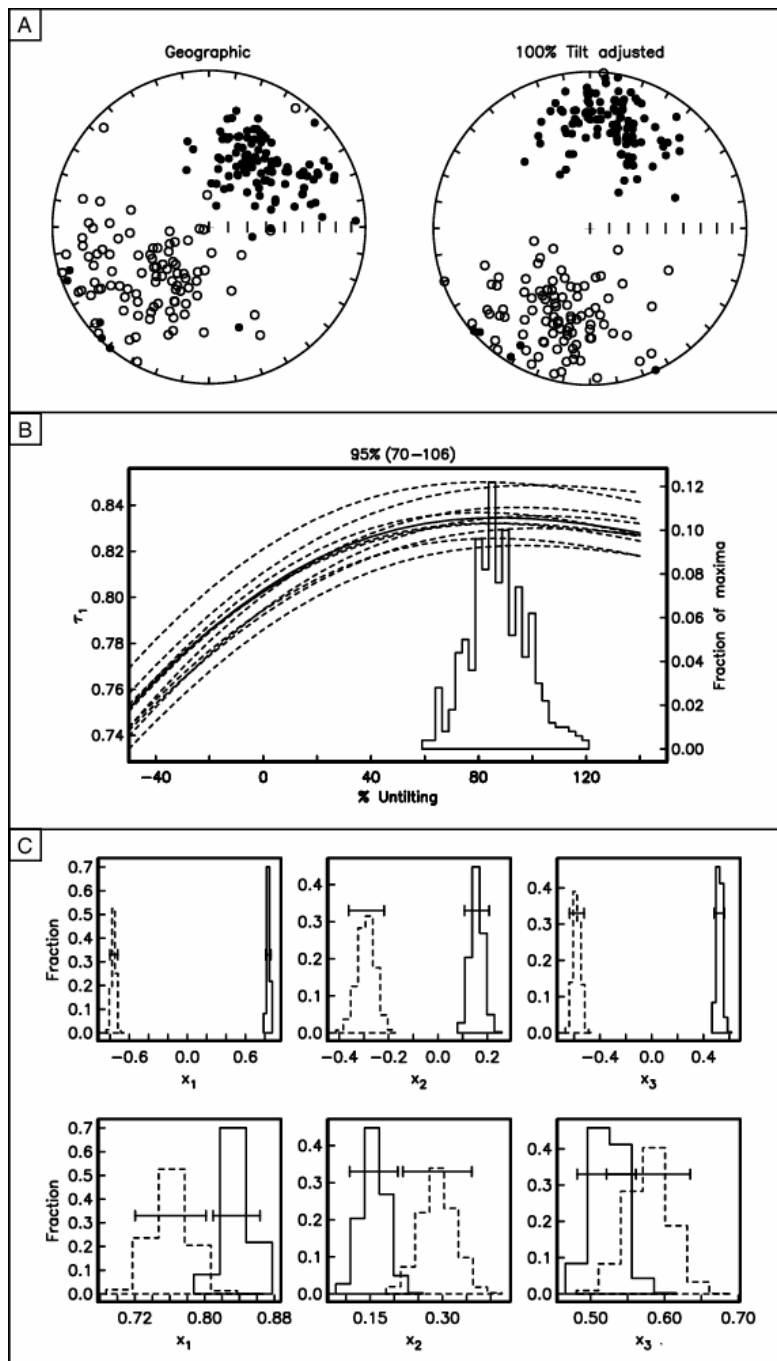
Additional references cited in the supplementary information

p. 12

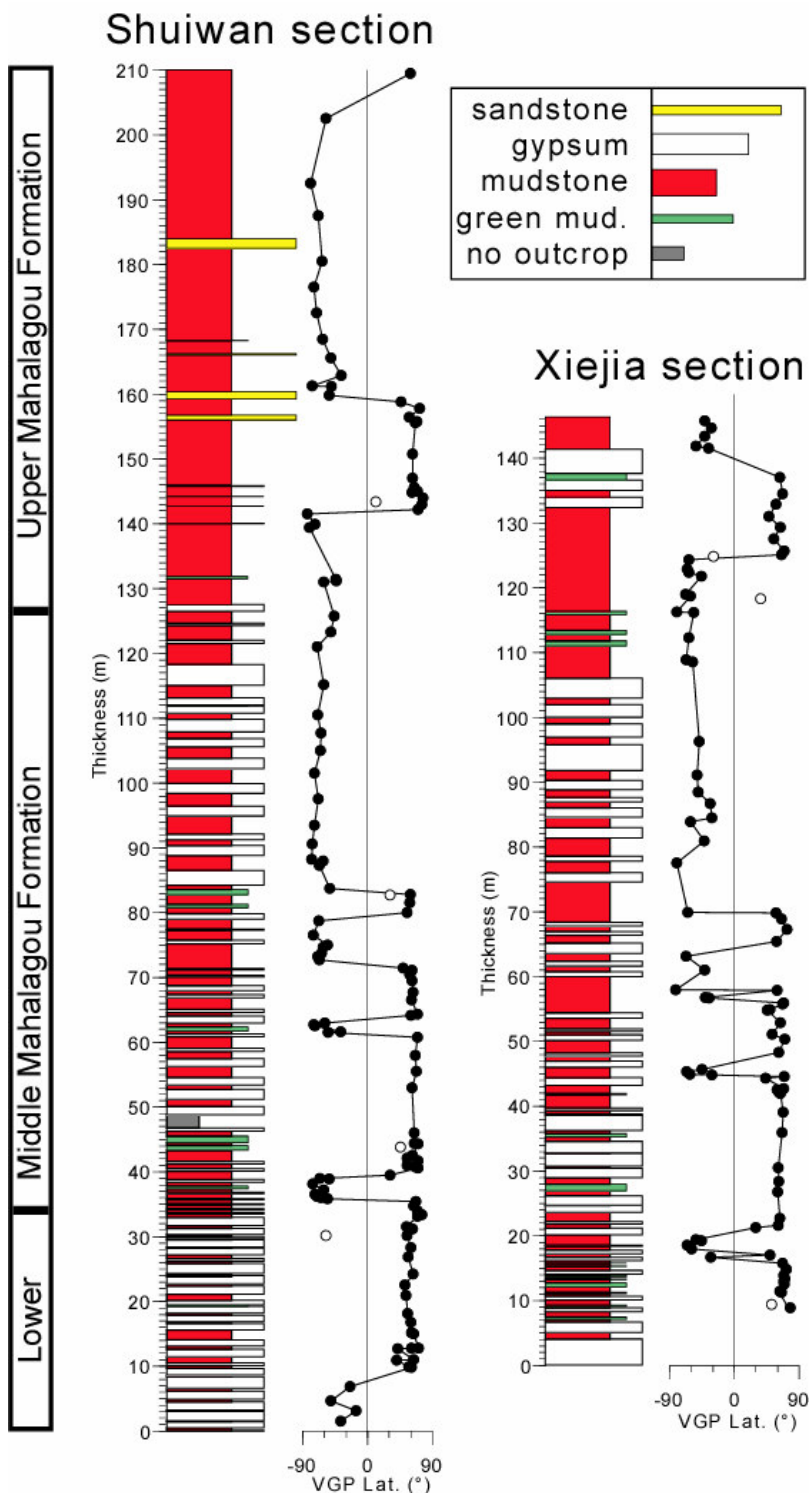
Supplementary figures



Supplementary Figure 1. Characteristic thermal demagnetization behaviours. Vector end point-diagrams (above) and associated decay curves (below) of the two characteristic behaviours (A and B). On vector end point-diagrams, open (full) dots are projection on the vertical (horizontal) plane. Stepwise thermal demagnetization at up to 19 steps and remanence measurements were carried out on 267 samples in a magnetically shielded oven and a 2G 755 DC cryogenic magnetometer at the Utrecht University Palaeomagnetic Laboratory. Most samples displayed similar characteristic behaviour (**A**): after removal of a low temperature component below 250°C , characteristic remanent magnetization (ChRM) directions decay linearly reaching the origin at ca. 620°C pointing to magnetite or maghemite carriers. Further linear decay until 670°C observed on a few samples (**B**), suggests the occasional presence hematite in addition to magnetite (or maghemite). The ChRM directions were assessed on vector end-point diagrams and calculated using least square line analysis³¹ estimating the maximum angular deviation (MAD) on a minimum of four measurements. Only two directions with erratic high temperature behaviour but clear reversed polarity have been calculated by forcing line fits through the origin. Fifty four samples showing erratic demagnetization behaviour resulting in ChRM directions with a maximum angular deviation above 30° were systematically rejected for further analysis. High-quality directions were obtained from the remaining 213 samples with average MAD value of 10.3° (Supplementary Tables 1 and 2).



Supplementary Figure 2. Characteristic remanent magnetization (ChRM) directions and field tests applied to both sections. **A**, ChRM directions before (geographic) and after tilt correction (100% tilt adjusted); Open (full) dots are upper (lower) hemisphere projection. The 206 ChRM directions from both sections cluster in nearly antipodal direction after correction of bedding tilt. **B**, The applied fold test³² is positive at the 95% confidence level. **C**, The dataset, however, closely fails the reversals test³² at 95% confidence level due to an offset (7.0°) between the mean normal and mean reverse directions. This slight offset, interpreted to result from an unresolved overlapping normal component, does not affect the reliability of the polarity determination clearly indicated by the Virtual Geomagnetic Pole latitudes (VGP lat.) calculated from the ChRM directions (Supplementary Figure 3).



Supplementary Figure 3. Magnetostratigraphy and lithostratigraphy of Shuiwan and Xiejia sections. Magnetostratigraphic data are given by virtual geomagnetic pole latitude (VGP lat.). White dots indicate discarded palaeomagnetic directions from the magnetostratigraphic analysis (open symbols) including six aberrant directions and one isolated apparent reversed polarity direction from the Shuiwan section (level 30.2 meter) where level re-sampling yielded normal polarity direction.

Supplementary tables

Supplementary Table 1. Lithofacies and paleoenvironment interpretations.

Fm.	Lithofacies Description	Depositional environment ³³⁻³⁸
Upper Mahalagou	<p><i>Red mudstone successions.</i></p> <p>Red mudstones consist of silty clays devoid of water stratification and showing only few sedimentary structures. Fine wavy textures and sub-millimetric interstitial gypsum growth preserved in the clastic mud are present (readily distinguished by their white colour upon heating above 350 °C during thermal demagnetisation). Parts of the section show cyclic alternations (~2 metres intervals) in interstitial gypsum content expressed by induration variations of the mudstone. Some of these more gypsiferous mudstone intervals show turbation features (undulating surface, and decimetric pseudo-anticline structures). Occasional cross-bedded fine to medium sandstones and yellow to brown colour mottling and striate occur sporadically within the mudstone successions.</p>	<p><i>Distal alluvial fan.</i></p> <p>These sediments were deposited in shallow ephemeral water bodies during flood events. The lack of sedimentary structures and the oxidised red colour indicate severe alteration after deposition during subsequent sub-aerial exposure. Relics of turbation features suggest repeated drying and wetting. Cyclic alternations of interstitial gypsiferous content reflects fluctuating water level and brine concentration not exceeding the threshold level required for the generation of massive gypsum layers. The absence of organic matter, reduced mudstones and massive gypsum layers indicates dominantly sub-aerial environment with occasionally very ephemeral and hypersaline sub-aqueous environment. Occasionally, larger flood events from distal alluvial provenance generate sandstones. Rare mottling is indicative of incipient pedologic processes during sub-aerial exposure.</p>
Middle Mahalagou	<p><i>Intercalations of red mudstone and gypsiferous horizons.</i></p> <p>Red mudstone intervals resemble red mudstone of the Upper Mahalagou formation (above). They consist of decimetre- to metre-thick homogenous silty clay intervals containing in places gypsum nodules. Aside from rare ripple development, mudstone intervals are devoid of sedimentary structures. Gypsiferous intervals are tabular decimetre- to metre-thick beds of alabastrine, massive, nodular and sometimes laminar gypsum including chickenwire structures and displacive enterolithic veins. Occurrences of mirabilite are reported³⁹ Gypsum layers can grade laterally to green mudstone showing occasionally preserved laminated layering and millimetric lenses of black organic matter. Individual beds and interval patterns can be correlated over large (>10 km) distances across the basin.</p>	<p><i>Distal alluvial fan and shallow playa lake alternations.</i></p> <p>Red mudstone intervals are interpreted as distal alluvial fan deposits (see above). Gypsum layers are indicative of various stages of chemical precipitation in the playa lake environment. A range of gypsiferous deposits indicate variations of sulphate concentration in water supplied by surface run-off and groundwater water driven by capillary action and evaporative pumping. Relative to mudstone intervals, gypsum layers correspond to higher water supply maintained for sufficient time to provide enough solute to accumulate meter-scale gypsum layers. Consistently, a deep and more perennial lake environment is indicated by preserved lamination and organic matter in green layers correlative to the gypsum layers. Gypsum/mudstone alternations indicate cyclic fluctuations in water supply to a regionally extensive system.</p>

Note: Lithofacies description of formations (Fm.) and inferred depositional environments.

Supplementary Table 2. Shuiwan section ChRM directions.

Sample	Level	Dg	Ig	Ds	Is	MAD
	(m)	(°)	(°)	(°)	(°)	(°)
HZ152.1	1.50	208.0	-2.9	210.8	14.2	12.3
HZ153.2	3.15	249.3	3.7	250.0	-1.2	2.1
HZ154.1	4.70	218.6	-28.4	207.6	-13.1	10.8
HZ155.1	6.90	265.1	-19.9	250.6	-29.5	2.3
HZ157.1	9.80	8.8	42.7	358.9	15.5	8.5
HZ157.2	9.90	21.7	34.3	11.8	11.6	4.3
HZ158.1	10.90	65.6	27.4	49.3	25.4	27.4
HZ8.2	11.00	26.9	47.7	15.4	27.3	13.9
HZ159.1	12.70	58.2	25.3	44.7	19.8	29.9
HZ159.2	12.80	12.9	40.8	2.5	14.8	11.8
HZ9.2	12.80	28.5	58.5	12.0	37.8	10.3
HZ10.1	15.00	35.8	51.1	20.3	32.5	11.3
HZ160.2	15.20	10.0	41.2	0.3	14.4	9.6
HZ11.2	16.75	36.4	46.5	22.7	28.4	9.8
HZ12.2	18.10	37.7	40.0	26.3	22.7	8.2
HZ13.1	20.90	13.2	24.7	10.5	2.3	13.6
HZ14.1	22.50	45.4	39.0	32.8	24.1	9.0
HZ15.2	24.20	19.9	44.7	11.2	23.0	5.8
HZ17.1	26.90	9.7	30.5	6.3	7.5	5.5
HZ18.1	28.30	17.7	39.3	11.0	17.4	14.1
HZ19.1*	30.20	164.5	-41.1	164.6	-16.1	9.2
HZ163.2	30.20	12.0	29.6	5.9	4.0	27.7
HZ167.1	31.20	69.5	52.6	31.1	46.2	22.7
HZ20.1	31.50	30.0	33.8	22.4	14.8	7.4
HZ21.1	33.10	34.6	55.4	15.6	37.4	10.1
HZ21B.1	33.40	21.3	61.3	4.4	40.0	4.2
HZ22.1	34.00	33.2	47.6	350.6	32.8	7.3
HZ23.2	34.75	28.1	46.5	15.3	27.6	4.4
HZ24.2	35.40	32.1	52.3	15.6	33.9	6.5
HZ169.1	35.85	182.7	-33.1	177.2	-4.9	12.0
HZ169.2	36.00	204.5	-46.5	188.1	-23.4	17.0
HZ25.2	36.20	208.4	-55.0	191.9	-35.5	5.0
HZ170.1	36.50	204.5	-60.6	180.1	-35.7	12.1
HZ26.1	37.20	240.9	-55.9	212.1	-45.5	12.6
HZ27.1	38.10	244.5	-87.0	167.0	-64.5	11.4
HZ174.1	38.90	200.6	-27.4	193.8	-4.9	17.3
HZ28.1	39.00	196.7	-47.6	186.7	-26.1	6.8
HZ175.1	39.45	229.7	-5.5	228.5	1.2	13.6
HZ177.1	40.60	52.1	56.6	17.5	41.5	11.1
HZ29.1	40.80	29.2	50.5	14.4	31.6	5.4
HZ178.1	41.00	30.5	32.3	19.4	13.0	28.0
HZ179.1	41.70	24.4	55.1	3.4	31.0	8.1
HZ180.1	42.10	26.2	30.9	16.7	10.1	24.7
HZ30.2	42.50	44.3	50.4	24.9	35.6	5.2
HZ181.2*	43.80	338.0	28.0	337.2	-3.8	15.3

HZ31.2	44.30	10.1	53.9	0.2	31.1	7.2
HZ182.2	44.40	50.4	50.9	21.6	36.6	13.6
HZ32.2	46.00	58.3	58.7	28.1	46.9	8.8
HZ35.1	53.00	50.0	51.9	27.9	38.7	10.2
HZ36.2	55.50	27.4	52.3	12.4	32.8	4.6
HZ37.2	58.00	47.2	55.8	23.4	41.1	7.9
HZ38.2	60.75	7.8	53.1	358.9	30.0	7.9
HZ39.2	61.50	235.7	-46.9	215.1	-36.2	4.6
HZ183.2	61.60	240.6	-20.2	229.6	-16.9	27.1
HZ184.1	62.50	224.9	-58.9	191.8	-40.6	12.4
HZ40.1	62.70	193.0	-61.1	179.6	-38.5	5.6
HZ184.2	62.95	201.4	-37.8	190.0	-14.7	29.3
HZ185.1	64.15	27.1	39.9	13.2	18.5	21.2
HZ41.2	64.30	16.2	52.4	4.8	30.6	8.4
HZ42.1	66.50	18.7	38.7	10.8	18.0	3.8
HZ43.2	67.70	23.0	44.2	12.4	24.3	13.0
HZ44.2	69.50	33.3	45.4	19.6	27.9	5.1
HZ186.1	70.40	6.8	38.5	358.8	11.0	9.6
HZ45.2	70.80	23.2	37.9	14.7	18.3	6.5
HZ186.2	71.10	47.3	46.1	23.3	31.6	10.9
HZ187.1	71.40	76.6	43.1	45.4	43.1	9.8
HZ188.1	72.70	227.1	-52.1	198.7	-36.2	16.5
HZ188.2	73.20	198.5	-56.4	179.3	-30.6	18.3
HZ46.1	73.70	247.8	-61.0	211.5	-51.7	6.9
HZ189.1	74.70	195.5	-41.7	184.1	-16.4	6.0
HZ189.2	75.00	199.1	-30.6	191.2	-7.3	7.5
HZ47.2	76.50	246.4	-70.7	198.3	-57.8	8.5
HZ48.2	78.70	231.1	-58.9	203.6	-44.9	9.0
HZ190.1	80.00	32.6	32.9	20.7	14.5	14.3
HZ191.1	81.50	27.4	37.0	14.8	16.0	8.1
HZ192.1*	82.70	132.6	48.9	92.9	75.8	17.6
HZ49.2	82.80	346.0	43.0	344.6	18.1	3.3
HZ193.1	83.70	130.7	-67.6	141.5	-36.5	12.6
HZ194.1	87.30	244.8	-55.9	204.9	-46.2	10.8
HZ50.2	88.00	224.2	-49.5	205.3	-34.8	6.0
HZ195.1	88.20	221.6	-63.9	185.7	-43.2	8.8
HZ51.2	90.60	185.6	-67.4	173.3	-43.6	8.7
HZ52.2	93.50	226.0	-63.9	196.6	-47.6	9.8
HZ53.2	97.50	208.0	-52.8	192.6	-33.4	11.4
HZ54.2	101.50	214.3	-60.7	192.4	-42.0	8.0
HZ55.2	105.00	223.8	-54.3	202.2	-38.9	14.4
HZ56.2	107.70	205.1	-46.7	193.0	-27.1	10.1
HZ57.1	110.50	204.0	-53.2	189.7	-32.9	7.1
HZ58.2	115.20	204.9	-40.4	195.2	-21.1	4.2
HZ59.2	121.00	189.7	-53.4	180.1	-30.6	5.1
HZ60.2	123.30	152.4	-36.8	153.8	-12.0	6.9
HZ61.2	125.80	154.6	-24.6	155.1	0.3	7.3

HZ62.1	131.00	249.4	-58.7	214.8	-50.5	7.0
HZ196.1	131.20	239.2	-28.0	223.9	-22.5	14.7
HZ196.2	131.40	282.4	-47.7	239.3	-59.7	7.0
HZ197.1	139.40	246.7	-67.7	190.4	-53.6	11.4
HZ197.2	139.90	194.0	-65.9	171.7	-38.0	12.6
HZ63.1	141.50	237.5	-77.2	185.5	-59.7	5.4
HZ198.2	142.20	3.1	67.1	346.1	37.4	4.3
HZ199.1	143.00	19.0	78.3	344.4	49.3	8.7
HZ64.2*	143.40	209.0	53.2	247.8	63.1	8.8
HZ199.2	144.00	28.0	66.7	357.4	41.7	12.7
HZ200.1	144.80	91.1	57.6	35.7	59.2	25.0
HZ65.2	145.00	31.7	54.6	14.1	36.0	8.4
HZ200.2	145.60	74.3	56.1	29.7	50.5	15.8
HZ66.2	147.00	34.8	46.2	20.3	29.0	13.1
HZ67.1	150.80	348.5	48.0	346.2	23.2	5.2
HZ68.2	155.60	20.0	48.2	8.9	27.3	8.3
HZ201.1	155.80	9.1	59.2	352.6	31.0	17.4
HZ201.2	156.40	338.5	57.9	335.4	26.1	14.9
HZ202.1	157.80	10.1	67.1	349.2	38.4	18.0
HZ202.2	158.80	60.8	32.5	42.2	27.0	17.1
HZ203.1	159.80	212.7	-30.8	201.8	-12.6	15.0
HZ203.2	161.20	357.0	-73.3	127.4	-71.6	11.8
HZ69.2	161.30	174.1	-76.6	165.3	-51.8	4.0
HZ70.2	162.90	93.3	-57.6	118.1	-42.5	18.1
HZ71.2	165.60	223.6	-34.4	212.3	-20.9	6.0
HZ71B	168.50	160.5	-54.5	161.0	-28.5	11.2
HZ72	172.50	238.7	-65.4	201.8	-50.9	11.7
HZ73	176.50	208.3	-62.3	188.4	-40.9	12.5
HZ74	180.50	232.8	-55.4	207.4	-41.1	3.6
HZ75	187.50	263.9	-69.4	206.8	-60.8	3.1
HZ76	192.50	259.9	-85.1	173.3	-64.2	3.8
HZ78	202.50	213.6	-41.0	201.9	-22.6	3.0
HZ79	209.50	102.6	66.8	38.6	66.1	4.2

Notes: Dg, Ig (Ds, Is) - declination and inclination in geographic (stratigraphic) coordinates; MAD – Maximum angular deviation³¹. * discarded direction.

Supplementary Table 3. Xiejia section ChRM directions.

Sample	Level	Dg	Ig	Ds	Is	MAD
	(m)	(°)	(°)	(°)	(°)	(°)
XJ49.2	8.90	45.4	43.0	347.2	49.8	5.1
XJ48.1*	9.40	86.5	30.4	47.0	75.4	2.3
XJ84.2	11.30	28.9	47.9	353.2	25.1	9.0
XJ84.1	11.40	31.7	36.5	4.6	20.2	13.9
XJ83.2	12.50	43.7	41.4	5.7	30.7	2.3
XJ83.1	13.00	70.5	36.5	23.2	47.2	27.3
XJ47.2	13.40	28.3	31.8	353.9	32.9	4.7
XJ46.1	13.90	24.7	31.7	352.2	30.2	16.9
XJ45.1	14.80	54.2	49.6	337.7	56.7	4.1
XJ43.1	15.80	24.4	24.9	358.6	26.3	23.4
XJ82.2	16.70	252.7	-2.2	240.4	-28.4	9.6
XJ82.1	17.00	313.4	-8.4	315.6	40.2	13.1
XJ42.1	18.00	240.0	-14.0	215.1	-46.4	6.5
XJ41.2	18.60	233.8	-54.2	149.4	-56.3	3.6
XJ81.2	19.20	261.5	-19.7	231.8	-46.7	6.5
XJ81.1	19.40	251.6	-23.4	219.8	-41.6	10.9
XJ80.2	21.30	87.6	6.9	70.2	41.7	6.4
XJ80.1	21.60	77.1	30.8	34.5	49.7	11.9
XJ40.2	22.70	48.9	45.4	346.8	24.5	9.6
XJ39.1	26.80	36.5	33.3	358.8	14.0	7.0
XJ38.2	28.40	64.4	23.5	15.2	23.1	1.2
XJ37.3	30.50	63.4	23.5	15.4	22.2	3.9
XJ36.2	35.90	47.0	39.9	5.2	25.7	6.0
XJ35.1	39.10	46.0	46.7	357.7	27.2	6.2
XJ79.2	41.95	60.2	31.7	23.8	37.5	6.0
XJ79.1	42.20	62.7	29.9	27.2	38.3	11.5
XJ78.2	42.40	59.5	30.5	24.7	36.4	23.7
XJ34.2	42.50	29.4	58.9	341.4	22.0	10.2
XJ78.1	42.70	52.7	37.1	14.2	34.6	6.5
XJ77.2	44.35	45.4	5.7	37.8	10.9	12.7
XJ77.1	44.60	55.0	38.3	14.0	36.8	10.1
XJ76.2	44.80	282.6	-18.6	257.3	-60.0	9.6
XJ33.2	44.90	269.5	-26.8	215.2	-56.2	3.3
XJ75.2	45.30	232.7	-35.0	196.5	-33.6	11.3
XJ75.1	45.70	283.3	-29.4	241.0	-68.2	19.5
XJ32.1	48.30	32.7	41.1	359.4	16.2	6.2
XJ31.1	50.30	67.6	34.6	16.8	39.8	19.4
XJ30.2	51.10	36.1	-6.7	5.0	-0.6	4.0
XJ29.2	52.90	39.2	42.9	359.8	21.3	4.1
XJ74.2	54.80	67.7	14.3	46.1	33.2	4.0
XJ74.1	54.90	60.0	16.2	39.0	28.6	6.2
XJ73.2	55.80	54.1	39.3	1.1	26.3	20.2
XJ73.1	55.90	67.5	52.0	345.8	34.9	11.3
XJ72.2	56.70	252.8	7.5	238.3	-30.9	20.2
XJ72.1	56.80	224.0	1.6	220.2	-7.0	15.8

XJ28.1	57.90	47.7	63.0	329.6	37.2	5.7
XJ71.2	58.00	262.8	-41.2	176.1	-47.8	18.8
XJ71.1	61.00	219.2	0.2	217.3	-3.0	17.6
XJ27.2	63.10	245.5	-32.5	198.9	-37.6	9.4
XJ70.2	65.40	69.4	15.8	30.7	36.2	9.3
XJ26.2	67.30	60.6	43.4	4.4	36.4	0.8
XJ69.2	68.90	60.1	33.4	21.8	38.2	9.2
XJ68.2	69.85	21.7	68.7	330.8	32.9	7.0
XJ68.1	69.90	236.6	-32.3	201.3	-35.1	9.0
XJ24.1	77.50	248.2	-49.8	180.5	-45.4	1.6
XJ23.2	80.90	243.5	-7.7	227.0	-25.1	5.0
XJ22.2	83.90	214.2	-34.5	187.2	-16.8	2.4
XJ21.1	84.50	228.8	8.3	231.1	-3.7	6.8
XJ20.1^	86.70	259.2	-7.9	241.8	-34.2	1.1
XJ19.1^	88.50	213.6	-16.7	203.2	-6.2	2.5
XJ18.2	91.10	240.3	-21.7	215.5	-29.1	2.5
XJ17.1	96.30	256.2	-22.0	225.8	-41.2	12.8
XJ67.2	108.60	225.6	-24.7	202.4	-22.9	5.5
XJ67.1	108.90	227.4	-37.0	191.8	-30.9	18.6
XJ14.2	112.30	214.7	-38.1	186.8	-20.4	6.5
XJ66.2	116.20	256.5	-27.5	218.5	-47.5	6.2
XJ12.2	116.30	265.7	-48.0	192.1	-58.1	5.5
XJ65.2*	118.30	207.6	27.1	232.4	23.4	6.3
XJ64.2	118.70	258.1	-31.1	214.8	-50.5	10.5
XJ64.1	119.00	214.3	-55.7	167.6	-32.0	25.3
XJ63.1	121.80	272.0	-24.2	236.1	-57.1	5.8
XJ62.2	122.40	272.2	-36.7	214.3	-63.5	6.7
XJ62.1	122.90	254.6	-34.6	207.9	-49.5	8.9
XJ61.2	124.30	230.3	-30.8	199.4	-29.7	5.8
XJ61.1*	124.80	137.7	46.7	254.2	79.8	12.4
XJ60.2	125.10	28.2	48.6	352.3	25.1	8.9
XJ60.1	125.70	70.7	36.9	22.8	47.5	8.4
XJ59.1	127.50	84.9	28.2	43.8	54.2	7.4
XJ58.1	129.30	77.4	33.8	30.6	51.2	6.3
XJ57.1	131.00	63.2	15.4	41.9	30.5	7.9
XJ56.1	132.90	11.9	42.2	349.8	12.2	21.8
XJ55.1	134.50	65.4	63.6	330.9	57.7	17.6
XJ54.1	137.00	33.2	48.1	359.0	19.8	18.0
XJ53.2	141.50	243.6	-10.0	231.6	-17.4	6.9
XJ53.1	141.90	163.3	33.5	159.4	-10.3	8.6
XJ52.1	143.40	244.2	-20.0	225.9	-20.9	4.2
XJ51.1	144.70	226.2	-2.6	226.7	3.8	22.7
XJ50.1	145.80	215.2	-12.9	211.6	4.1	25.6

Notes: Dg, Ig (Ds, Is) - declination and inclination in geographic (stratigraphic) coordinates; MAD – Maximum angular deviation³¹. * discarded direction. ^ forced line fit.

Supplementary Table 4. Correlations and rates.

Age reference		Shuiwan section		Xiejia section		
Chron	Age	Level	Rate	Age	Level	Rate
<i>GPTS</i>	<i>(Myrs ago)</i>	<i>(m)</i>	<i>(cm/kyr)</i>	<i>(Myrs ago)</i>	<i>(m)</i>	<i>(cm/kyr)</i>
B_C18n.2n	39.464	8.35		39.464		
T_C18n.1n	38.032	35.63	1.9	38.032	16.25	
B_C17n.3n	37.771	40.03	1.7	37.771	20.35	1.6
T_C17n.1n	36.512	61.13	1.7	36.512	44.70	1.9
B_C16n.2n	36.276	63.55	1.0	36.276	47.00	1.0
T_C16n.1n	35.404	72.05	1.0	35.404	57.95	1.3
B_C15n	35.043	79.35	2.0	35.043	64.25	1.7
T_C15n	34.782	83.25	1.5	34.782	69.40	2.0
G_0	33.994	127.50		33.899	116.05	
B_C13n	33.738	141.85	5.6	33.738	124.55	5.3
T_C13n	33.266	159.30	3.7	33.266	139.25	3.1
B_C12n	31.116	206.00	2.2	31.116		
<i>APTS</i>	<i>(Myrs ago)</i>	<i>(m)</i>	<i>(cm/kyr)</i>	<i>(Myrs ago)</i>	<i>(m)</i>	<i>(cm/kyr)</i>
T_C15n	35.126	83.25		35.126	69.40	
G_0	34.053	127.50		33.945	116.05	
B_C13n	33.705	141.85	4.1	33.705	125.55	4.0
T_C13n	33.157	159.30	3.2	33.157	139.25	2.5
B_C12n	31.034	206.00	2.2	31.034		

Notes: Age reference- Age of bottom (B_) and top (T_) boundaries of Chrons are given according to the GPTS²⁰ and APTS^{7,40}. The age of G_0, the highest correlatable gypsum layer defining the lithologic change, is calculated through linear interpolation between T_C15n and B_C13n. Correlated levels of observed polarity zone boundaries at the Shuiwan and Xiejia section are given in meters (m) with associated sediment accumulation rates in centimetres per thousand years (cm/kyr) interpolated between chron boundaries.

Additional references cited in the supplementary information

31. Kirschvink, J. L. The least-square line and plane and the analysis of paleomagnetic data. *Geophysical journal of the Royal Astronomical Society* **62**, 699-718 (1980).
32. Tauxe, L. *Paleomagnetic principles and practice* (ed. Nolet, G.) (Kluwer Academic Publisher, Dordrecht/Boston/London, 1998).
33. Abdul Aziz, H., Sanz-Rubio, E., Calvo, J. P., Hilgen, F. J. & Krijgsman, W. Palaeoenvironmental reconstruction of a middle Miocene alluvial fan to cyclic shallow lacustrine depositional system in the Calatayud Basin (NE Spain). *Sedimentology* **50**, 211-236 (2003).
34. Lowenstein, T. K. & Hardie, L. A. Criteria for recognition of salt-pan evaporites. *Sedimentology* **32**, 627-644 (1985).
35. Reinhardt, L. & Ricken, W. The stratigraphic and geochemical record of Playa Cycles: monitoring a Pangaeen monsoon-like system (Triassic, Middle Keuper, S. Germany). *Palaeogeogr. Palaeoclimatol. Palaeoecol.* **161**, 205-227 (2000).
36. Rosen, M. R. in *Paleoclimate and Basin Evolution of Playa Systems: GSA special paper 289* (ed. Rosen, M. R.) 112 (1994).
37. Schreiber, B. C. & Tabakh, M. E. Deposition and early alteration of evaporites. *Sedimentology* **47**, 215-238 (2000).
38. Talbot, M. R. & Allen, P. A. in *Sedimentary Environments: Processes, Facies and Stratigraphy* (ed. Reading, H. G.) 83-124 (Blackwell Publishing Inc., 1996).
39. Qinghai Bureau of Geology and Mineral Resources. *Geologic maps of the Duoba, Gaodian, Tianjiazai, and Xining regions (4 sheets), with regional geologic report (1:50,000 scale)* (Geological Publishing House, Beijing, 1985).
40. Pälike, H. et al. in *Proceedings of the Ocean Drilling Program, Scientific Results* (eds. Wilson, P. A., Lyle, M. & Firth, J. V.) 1-41 (2005).